

Experimental characterization of a Partially Stirred Reactor (PaSR)

by

B. Renou⁽¹⁾, J-F Krawczynski, B. Le Naour, F.-X. Demoulin⁽²⁾, and L. Danaïla⁽³⁾

UMR 6614 CORIA

INSA - Avenue de l'Université - BP8

76801 Saint-Etienne-du-Rouvray Cedex

France

⁽¹⁾E-Mail: Renou@coria.fr

⁽²⁾E-Mail: Demoulin@coria.fr

⁽³⁾E-Mail: Danaïla@coria.fr

ABSTRACT

Simultaneous PIV and acetone PLIF measurements are conducted to characterize experiments designed to approximate an ideal, Partially Stirred Reactor (PaSR). The PaSR is an useful tool to develop and validate models for turbulent phenomena, such as micromixing models for PDF methods. Such methods can, in principle, represent the coupling between mixing and chemical processes, with chemical source terms exactly calculated. Initial results (Figure 1) are in a non-reactive configuration and document the capabilities to determine statistical information concerning the PaSR velocity and scalar fields, such as length scales, scalar gradient, scalar PDF etc. Global approaches to represent an ideal PaSR are discussed, and a particular attention is paid to a proper determination of the mean value of the passive scalar variance dissipation rate, $\overline{\epsilon_Z}$.

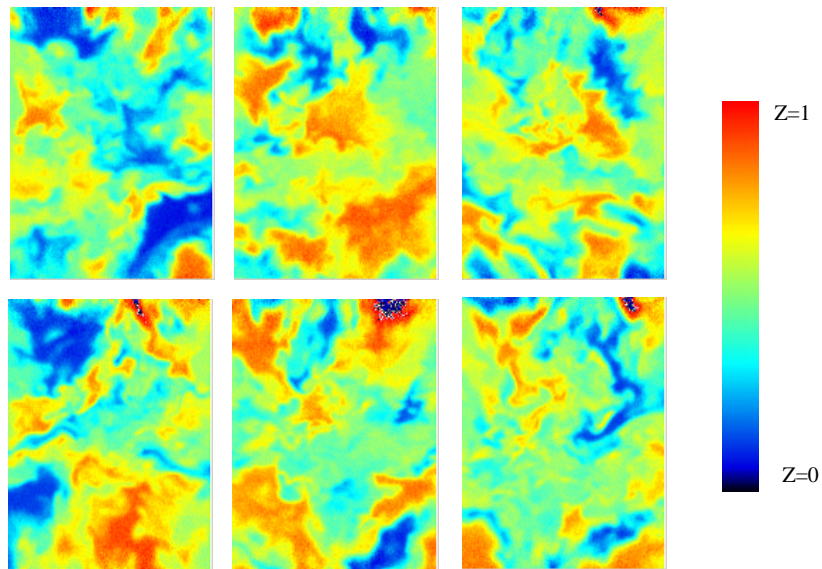


Fig. 1. Instantaneous scalar fields obtained by acetone PLIF.

1. INTRODUCTION

Understanding of combustion phenomena in a car engine, for example, must cover new technologies such as HCCI (Homogeneous Charge Compression Ignition) combustion. In an idealized configuration, HCCI combustion can be described as controlled auto-ignition of a global homogeneous fuel/air mixture that occurs without flame-front propagation. To have a globally homogeneous mixture, long mixing times between the fresh charge and the fuel (early fuel injection) are desirable. In this case, while homogeneity is assumed at large scales, fluctuations still exist at small scales. Optimal HCCI engine operation requires accurate control of temperature, pressure, auto-ignition delays, chemical composition, and micromixing. Christensen et al. (1998) have underlined that the understanding of the coupling between mixing and chemical processes is of first importance since it controls the combustion phenomena.

Combustion phenomena occur in a turbulent medium, which could be described for such configurations by statistical approaches. The transport equations for statistical quantities, such as mean, pdf, etc., include a micromixing term that represents mixing at small scales. Modeling of this micromixing term and its coupling with representative kinetic schemes is one of the main goals in HCCI combustion modeling and, more generally, an important objective of PDF methods (Ren and Pope 2003).

The objective of this work is to provide an experimental tool to test, validate, and develop micromixing models in a configuration close to the HCCI engines. This configuration can be represented by an idealized PaSR, characterized by a homogeneous medium at large scales, with local scalar and velocity inhomogeneities at small scales (Correa 1993).

In the experiments reported here, the PaSR is characterized with simultaneous PIV and acetone PLIF measurements. These provide statistical information on the scalar field, e.g., mean, statistical moments, dissipation, and velocity field. These initial results are presented as a first step in the analysis of PaSR applications in reactive flows.

The paper is organized as follows: after presenting the experimental set-up (Section 2), simultaneous velocity-scalar measurement results are discussed (Section 3.1). Passive scalar mixing is further characterized (Section 3.2), with the aim of inferring $\overline{\varepsilon_z}$ as accurate as possible. For that, different methods are employed: the spectral method, the correlation method, finite differences and the structure functions. Conclusions are finally drawn.

2. EXPERIMENTAL SET-UP

The PaSR consists of cubic box (4 cm^3), equipped with optical access ($24\times 24\text{ mm}$), in which a turbulent flow that is approximately homogeneous and isotropic is realized. Since no actual flow can satisfy all conditions of isotropy, the best one can achieve experimentally is a flow that is nearly isotropic, stationary, and homogeneous.

The most common way to generate nearly isotropic turbulence is using conventional (static) grid turbulence (Comte-Bellot and Corrsin 1966). Despite its popularity and success, it has several limitations that are difficult to overcome (relatively small Reynolds numbers, large wind tunnels etc.). Active grid turbulence allows for much larger Reynolds numbers (Mydlarski and Warhaft 1996).

Other recent methods to generate isotropic turbulence include the use of closed vessels stirred with fans (Birouk et al. 2003, Hwang and Eaton, 2003, and references therein). Compared with decaying grid turbulence, where the turbulence intensity is (maximum) 3%, closed-vessel turbulence is characterized by high turbulence intensity (up to 100%), partly because of low mean velocity.

In the present work, a different approach is used. The task at hand is more difficult, since the aim is to create nearly isotropic scalar mixing. That necessarily requires a nearly isotropic velocity field. The reactor used is 'partially stirred' since the velocity and the concentration fluctuate around a constant mean value. To keep the fluctuation level constant, fluid is continuously introduced to the box interior, through 12 inlets located on two opposite planes (Figures 2 and 3). Outlets are also situated in these two opposite planes.

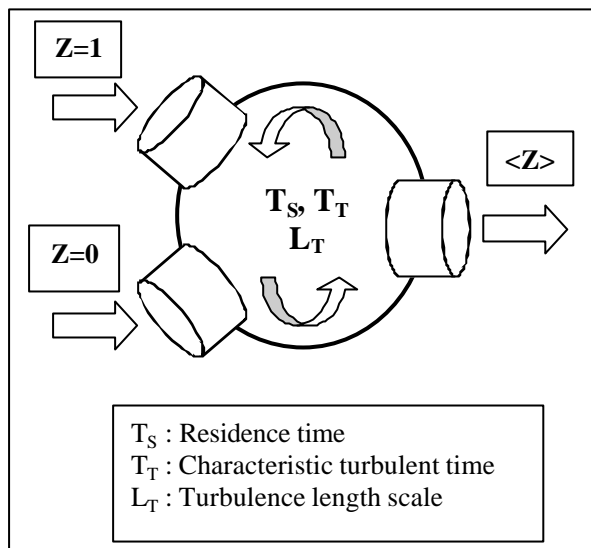


Fig. 2. PaSR schematic.

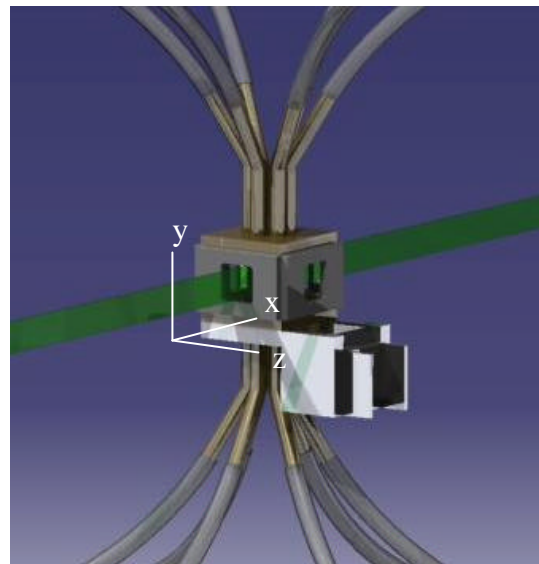


Fig. 3. Actual experimental PaSR

Two different fluids are introduced with an identical flow rate, to evaluate the mixing phenomenon : air ($Z=0$) and air doped with 2% by volume of acetone ($Z=1$).

The scalar field is measured by Planar Laser Induced Fluorescence on acetone (Lozano et al., 1992 ; Bryant et al. 2000). Efficient excitation of large planar sheets of fluid containing acetone vapors may be readily achieved using UV Excimer laser (KrF) at 248nm. The effects of laser sheet attenuation are minimized by using a low acetone concentration (2% in volume) in air.

Two cylindrical lenses are used to obtain a laser sheet of 0.5 mm by 50 mm, with a typical pulse energy of 150mJ. Linearity of fluorescence signal with energy has been verified in the range of 50mJ to 200mJ. The acetone fluorescence images are detected with 50 mm Nikkor lens (f:1/1.2) on an Intensified CCD camera (FlameStar LaVision, 14 bits), with a CCD array of 284×386 pixels² and a magnification scale of $9.4 \text{ pixels.mm}^{-1}$. A colored glass filter BG12 is used to suppress any scattered laser light. In order to obtain a quantitative measure of the scalar field, the images are corrected for a number of influences such as background and light-sheet profiles (van Cruyningen et al., 1990). The shot noise could be reduced by applying a 2×2 Wiener spatial filter (Brunel et al., 2002). This technique assumes that the noise present in the system is additive, white and Gaussian. The images treatment is done using Matlab 6.3.

In the next section, passive scalar images with no such a filter (hereafter, NF) will be critically compared with filtered images (using a Wiener 2×2 filter, hereafter, W22 images).

The velocity field is simultaneously measured by PIV. The PIV apparatus consists of a two-pulse frequency doubled Nd: YAG laser (Big Sky lasers, 120 mJ), with an interval time of $10 \mu\text{s}$. The scattered light from particles is collected onto a CCD camera (FlowMaster LaVision 12 bits), which allows the acquisition of two successive 1280×1024 pixel² images. The field of view of PIV images is fixed to $24 \times 24 \text{ mm}^2$, with a magnification scale of 37.8 pixels/mm.

3. EXPERIMENTAL RESULTS

3.1 Velocity and scalar preliminary results

The experiments are carried out following 9 parallel vertical planes (Figure 3) in order to evaluate the PaSR properties in the volume as a whole. For each plane, more than 200 PIV and PLIF images are recorded simultaneously. The residence time, T_S , determined from the ratio of the PaSR volume over the flow rate, is fixed at 8ms, which leads to a mean inlet velocity of 13.3m/s within the PaSR.

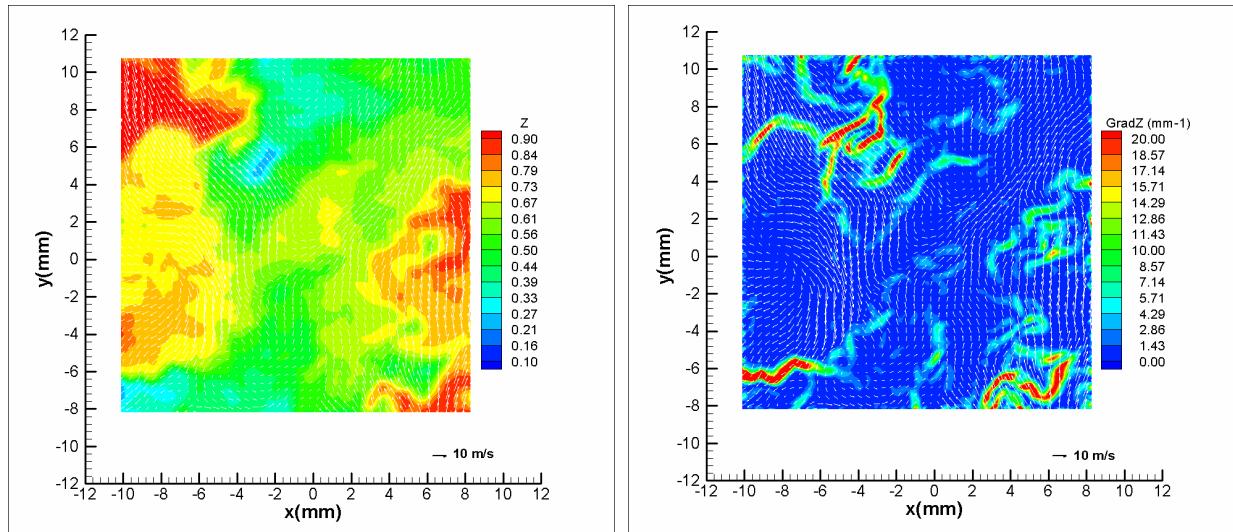
The primary objective is to provide detailed velocity properties such as r.m.s. velocities, spatial autocorrelations, integral length scales and spectra. The elementary statistics obtained from the velocity and the scalar fields are reported in Table 1.

Turbulence properties		Scalar properties	
u' (m/s)	2.97	Z'^2	0.03
v' (m/s)	2.46	Z	0.50
U (m/s)	1.31		
L_{Ux} (mm)	2.5	L_{Zx} (mm)	3.15
L_{Uy} (mm)	1.5	L_{Zy} (mm)	3.30
L_{Vx} (mm)	1.4		
L_{Vy} (mm)	3.5		

Table 1. Turbulence and scalar properties in the $z = 0\text{mm}$ plane.

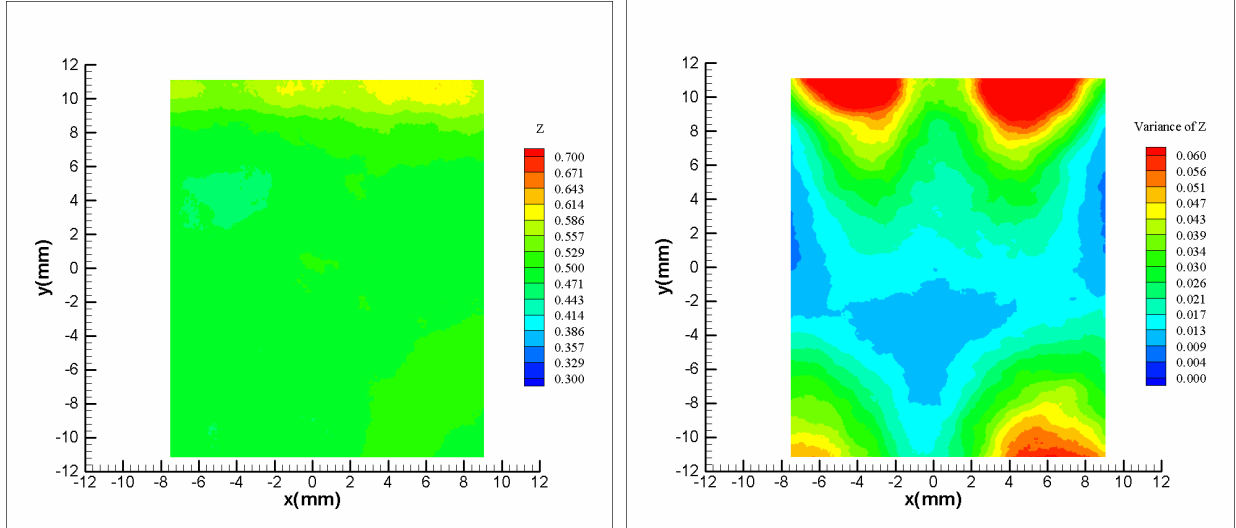
Transversal and longitudinal length scales are deduced from the autocorrelation coefficients of the velocity field and indicate that the turbulent flow can be considered (to a first approximation) as nearly isotropic since the classical relationship between the integral length scales $L_{Ux} \approx 2 L_{Uy}$ ($\approx 3\text{mm}$) very nearly observed. The r.m.s. velocities are roughly equal in all the planes. However, the mean flow velocity can not be neglected (18% of the inlet velocity). An improvement of the PaSR geometry is planned in order to reduce this residual mean velocity to smaller values.

Then, the experimental set-up and optical diagnostics allow the velocity and the scalar (and the scalar gradient) to be obtained simultaneously (Figures 4).



Figures 4: Instantaneous velocity field with the corresponding scalar field and the gradient scalar field.

Figures 5 illustrate a globally homogeneous mixing (the mean value of Z is 0.5 and the variance is about 0.03), though, as already recognized, small-scale inhomogeneities and anisotropies still persist. On the image of the variance (i.e. the scalar energy), injection zones are clearly discernible (top and bottom) corresponding to the high-energy inlets. The central zone, with a lower energy, corresponds to a 'still' zone, where the scalar is much better mixed.



Figures 5: Mean value of the scalar field (left) and the variance of its fluctuations (right). These images are obtained by time-averaging the scalar statistics at each point in the measurement zone.

3.2 Characterisation of the passive scalar mixing

After a first, rather global, characterization of the flow and of the mixing, our next goal is to determine an important parameter of (most) micro-mixing models: the mixing time T_m . This characteristic time is based on an accurate description of the scalar fields, and new sets of PLIF experiments are needed with a higher number of images (512) and a higher magnification ratio (17.4 pixel/mm).

The mixing time is to be experimentally determined, using one of its simplest definitions: $T_m = \overline{Z'^2} / \overline{\epsilon_z}$, where $\overline{Z'^2}$ is scalar the fluctuations variance and $\overline{\epsilon_z}$ is the mean dissipation rate of these fluctuations. Time averaging at each point of the domain is performed. Since global homogeneity is well respected, spatial averaging is also done, permitting rapid statistical convergence. We note that, if the passive scalar and the velocity field are injected in the same manner [e.g. at the same scales], T_m should be equal to the turbulence characteristic time: $T_t = \overline{q^2} / \overline{\epsilon}$, where $\overline{q^2}$ is (twice) the mean turbulent energy and $\overline{\epsilon}$ its dissipation rate. Whereas $\overline{q^2}$ and $\overline{Z'^2}$ can be classically obtained from our measurements, a proper estimation of small-scale quantities such as $\overline{\epsilon_z}$ or $\overline{\epsilon}$ usually hide more difficulties.

We concentrate our efforts on a proper determination of $\overline{\epsilon_z}$. This is the main goal of this paper. In the phase of validation of the experimental method, concerns are:

- (i) How contaminated are the small-scales by noise?
- (ii) Are the small scales well measured? Is spatial resolution adequate to provide reliable small-scale information?
- (iii) How to measure with accuracy the mean scalar dissipation?

These questions cannot be entirely separated. We will first discuss the first one.

(i) How much contaminated are the small-scales by the noise?

This task is addressed via spectral analysis. Indeed, the energy spectra analysis may be an interesting tool to evaluate the experimental minimum resolved scales, in comparison with theoretical spectra. For instance, the energy spectrum $E_z(k)$ can be used to determine the mean scalar dissipation $\overline{\varepsilon_z}$, relying on an isotropy hypothesis:

$$\overline{\varepsilon_z} \propto \int_0^{\infty} E_z(k) k^2 dk \quad (1)$$

This necessitates knowledge (measurement) of $E_z(k)$, to the highest wavenumbers, with good noise-decontamination. These two problems address the above-mentioned concerns.

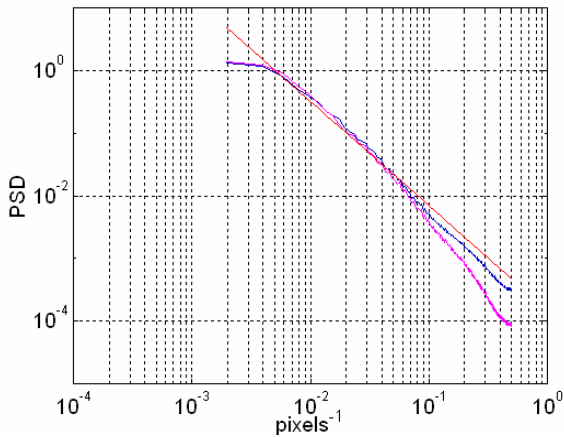


Figure 6 : Scalar, Z, power spectrum vs. estimated wavenumber $k \sim \text{pixels}^{-1}$: Blue: NF signal. Magenta: W22 signal. Red line indicates a $k^{-5/3}$ power law.

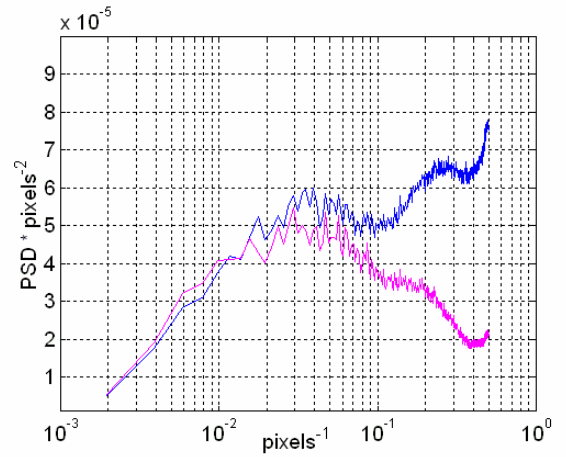


Figure 7: Compensated PSD, $k^2 E_z(k)$, that is integrated (from 0 to ∞) to yield $\overline{\varepsilon_z}$: Blue: NF signal. Magenta: W22 signal.

Figure 6 represents the PSD of the scalar Z, as a function of $k = \text{pixels}^{-1}$. We note here that the signal analyzed was obtained by considering all measured values of Z along the x direction, by considering all the horizontal lines of each image. Thus, the estimated wavenumber, k , is along the x direction, normal to jet-injection direction. Similar results are obtained when using the y direction, indicating that global homogeneity and isotropy are well approximated. Figure 6 illustrates that both measured spectra (NF and W22) present a restricted scaling range (hereafter, RSR), defined as the range for which $E_z(k) \sim k^{-5/3}$ (indicated by the red line), for a range given by 25-30 pixels (1.8 mm), i.e., approximately 1/10 of the image width and approximately half the integral scale. The RSR is restricted, as a direct consequence of the (relatively) low Reynolds number of the flow ($R_\lambda \approx 80$, where R_λ is the Taylor microscale Reynolds number). The spectra are quite similar, excepted at high wavenumbers. This agrees with the fact that the variance of the two signals, representing the areas under the spectra, are almost the same.

Figure 7 plots the compensated spectra $k^2 E(k)$, that must be integrated in order to obtain $\overline{\varepsilon_z}$. Note that the compensated spectrum for the NF signal does not decay to zero for higher and higher values of k , because of the noise contamination mainly at high wavenumbers. On the other hand, the W22 filtered signal has a good trend, and decays correctly. The difference between the two spectra is mainly (not entirely) attributable to noise. This spectral observation allows us to point out a *very first conclusion*: the W22 signal is more adapted (than the NF signal) to correctly infer small-scale information. The W22 signal is largely noise-decontaminated. However, even though the filtered signal is decaying well, it does not decay to zero, and even the high wavenumber portion of this spectrum must be modelled (Pao 1965, Elsner et al. 1993). This implies that even the W22 spectrum suffers from the pathology emphasized in concern (ii) e.g. the smallest scales of the mixing are not measured, the pixel size being larger than the smallest scale of the mixing. The answer to question (ii) is negative, and more precise measurements (higher CCD array, ...) would be necessary to better describe the very small scales of the mixing.

Under these conditions, we further address the main question of this study:

(iii): How to measure with accuracy the mean scalar dissipation ?

Different approaches can be used to determine the mean scalar dissipation, but each of them presents some drawbacks since, as previously discussed, the smallest scales of the flow /mixing are not measured. Moreover, different noises contaminate the PLIF images and may induce an over estimation of the mean scalar dissipation.

- The first and the most classical approach consists of using finite differences approximations according to the following relation:

$$\overline{\epsilon_Z} = D \left(\left(\frac{\partial \overline{Z}}{\partial x} \right)^2 + \left(\frac{\partial \overline{Z}}{\partial y} \right)^2 + \left(\frac{\partial \overline{Z}}{\partial z} \right)^2 \right)_{\text{FD}} \approx D \left(\left(\frac{\Delta Z}{\Delta x} \right)^2 + \left(\frac{\Delta Z}{\Delta y} \right)^2 + \left(\frac{\Delta Z}{\Delta z} \right)^2 \right) \quad (1)$$

The subscript FD denotes finite differencing. This allows to determine the mean scalar dissipation, noted $(\epsilon_Z)_{\text{FD}}$, by assuming isotropy:

$$(\epsilon_Z)_{\text{FD}} \equiv 3D \left(\frac{\partial \overline{Z}}{\partial x} \right)_{\text{FD}}^2 \quad (2)$$

where D is the molecular diffusion coefficient of the acetone in the air (the Sc number of the mixing is estimated as being approximately 1.3).

- We now chose to continue our investigation using another tool, that is the structure functions. Figure 8 depicts the normalized second-order structure functions, associated with the scalar increments: $\Delta Z = Z(x+r) - Z(x)$, where, as for the spectra, the signal is obtained by aligning all the horizontal lines of all images, so that the separation r is parallel to the x direction. The second-order structure functions are defined as:

$$S_2(r) = \overline{(Z(x+r) - Z(x))^2} \quad (3)$$

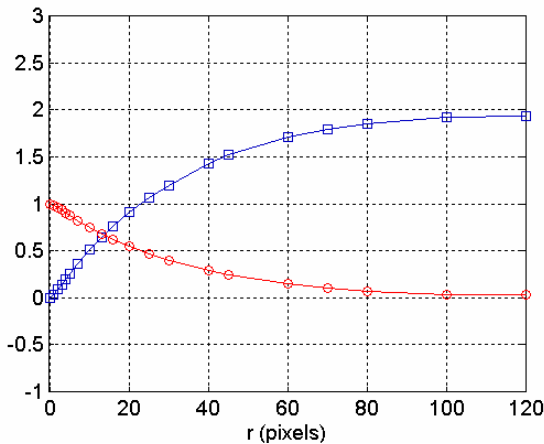


Figure 8: Normalised second-order structure functions $S_2(r)/\overline{Z^2}$ (blue) and the autocorrelation coefficient $r(r)$ (red).

We note that $\lim_{r \rightarrow \infty} S_2(r)/\overline{Z^2} = 2$. As Figure 8 illustrates, this limit is correctly reached for a scale of about 100 pixels ($\sim 6\text{mm}$), that therefore represents the scale for which there is vanishing correlation between the scalars. As 100 pixels represent 1/3 of the box width, and recalling that the injection is done by three jets for each side (upper and lower), it is not surprising to find that the scalar globally becomes uncorrelated from one jet to another one. This is the direct effect of the dependence on the initial (injection) conditions.

As for the spectra, the structure functions also exhibit a RSR, for which $S_2(r) \propto r^{2/3}$. This RSR is the same as the one discussed for the spectral analysis.

The mean scalar dissipation can be also obtained using the definition of the second-order structure functions (noted $(\epsilon_Z)_{SF}$) :

$$(\epsilon_Z)_{SF} = \lim_{r \rightarrow 0} \left(3D \frac{S_2(r)}{r^2} \right). \quad (4)$$

Figure 9 represents the ratio $3D \frac{S_2(r)}{r^2}$ for the NF signal (blue solid line and squares) as well as its limit for r going to zero (blue circle). The extrapolation for $r=0$ was calculated using a third-order polynomial function. The trend clearly emphasizes a rapid increase of $3D \frac{S_2(r)}{r^2}$ when the separation r goes to zero, thus emphasizing the difficulty in choosing an optimal separation, and thus the difficulty in estimating $(\epsilon_Z)_{SF}$. Also represented on Fig. 9 is the ratio $(3D \frac{S_2(r)}{r^2})$ calculated from the W22 signal (magenta solid line and squares). The extrapolation for $r=0$ (magenta circle) constitutes a much more reliable value of $(\epsilon_Z)_{SF}$, here noted $(\epsilon_Z)_C$, mainly because the signal is largely noise-decontaminated. This value of $(\epsilon_Z)_C$ is relatively close to $(\epsilon_Z)_{FD}$ (blue diamond), obtained from finite differences method and the NF signal.

- Another criterion, more objective, is further investigated to estimate the true value of $\overline{\epsilon_Z}$. For this purpose, we further investigate the correlation coefficient method. Since (global) homogeneity along the 3 directions is well satisfied in the present flow, the scalar signal presents almost the same variance in any two different points of the measurement zone. The correlation coefficient $\rho(r) = \frac{\overline{(Z(x) \times Z(x+r))}}{\overline{Z^2}}$ is also represented on Figure 8. The integral scale of the scalar field is of about 40 pixels, roughly representing the injection jet diameter. Performing a Taylor series expansion of the correlation coefficient $\rho(r)$ along the x direction (Eq. 5), the osculating parabola thus obtained is supposed to yield the derivative variance:

$$\rho(\Delta x) = 1 - \frac{1}{2} (\Delta x)^2 \frac{\left(\frac{\partial \overline{Z}}{\partial x} \right)_{Corr}^2}{\overline{Z^2}} + o\left[(\Delta x)^3 \right] \quad (5)$$

where the subscript ‘Corr’ denotes values obtained from the correlation method. This last quantity directly yields the value of $(\epsilon_Z)_{Corr}$, represented on Fig. 9 by a blue star. The value of $(\epsilon_Z)_{Corr}$ is intermediate between the values of $(\epsilon_Z)_C$ and $(\epsilon_Z)_{FD}$. However, in the case of our measurement, because of the fact that the size of a pixel is relatively large in comparison with the smallest scales of the velocity and scalar field, the correlation coefficient only presents a very restricted zone with a parabolic behaviour. Therefore, the correlation method is not the most reliable method.

- Another more reliable method for determining the variance of the scalar derivative along the x direction is (as already discussed) to noise-decontaminate the NF signal. Figure 9 indicates that the mean squared scalar difference is not zero when r goes to zero (this could also be seen on Figure 8, after doing a zoom for the very small separations). Following the procedure outlined in Anselmet et al. (1994) and Danaila et al. (2000), the residual noise $b^2 = \lim_{r \rightarrow 0} S_2(r)$ is first determined and subtracted from each $(\overline{\Delta Z})^2(r)$ value, to obtain a corrected value of the derivative variance, viz.

$$\left(\frac{\Delta Z}{\Delta X} \right)_C^2 = \frac{(\overline{\Delta Z})^2 - b^2}{r^2} \quad (6)$$

where the subscript ‘C’ refers to the corrected data. The noise-corrected data (blue solid line and diamonds) are compared with the W22 data (magenta line and squares) on Figure 9. The two curves are quite similar, at least for

the separations larger than 1 pixel, thus emphasizing the fact that the W22 is an useful tool to noise-decontaminate the NF (originally measured) signal.

The extrapolation to $r=0$ of the W22 noise-corrected values gives $(\epsilon_Z)_C$, represented on Figure 9 by a magenta open circle.

- Another possibility to determine $\overline{\epsilon_Z}$ is through its large-scale estimation. To do this, we write the transport equation of the scalar variance assuming mass conservation and homogeneity:

$$\overline{Z_E^2} - \overline{Z_I^2} = -T_r(\epsilon_Z)_{LS}, \quad (7)$$

where $\overline{Z_E^2}$ represents the scalar variance at the exit of the PaSR and is set equal to the scalar variance within the reactor, $\overline{Z_I^2}$ is the scalar variance imposed by the inlet conditions, T_r is the residence time, and $(\epsilon_Z)_{LS}$ is the mean scalar dissipation that must be modelled (using the large-scales method) to represent micro-mixing. From our acetone PLIF measurements, all the terms in Equation 7 can be experimentally obtained, thus determining the value of $(\epsilon_Z)_{LS}$.

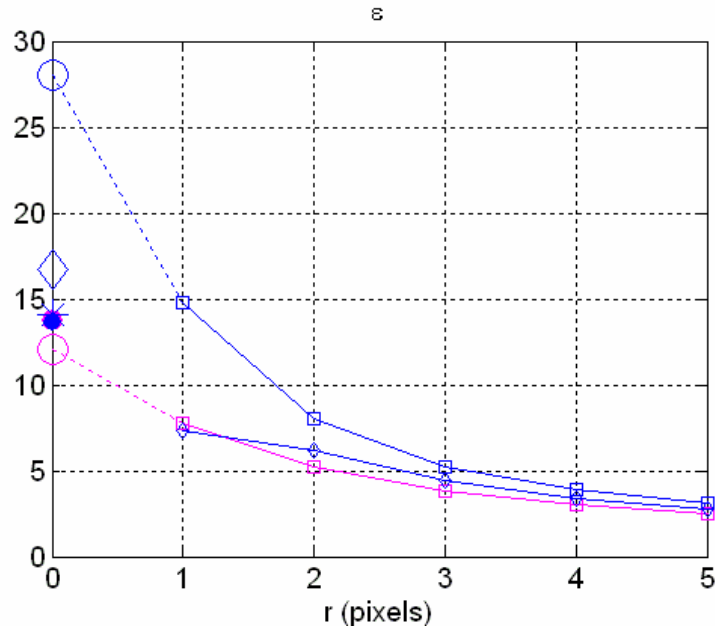


Figure 9 : Different methods of estimating ϵ_Z , as a function of separation r (pixels). Blue solid line and squares:

$3D \frac{S_2(r)}{r^2}$ from the NF signal. Blue \circ : $(\epsilon_Z)_{SF}$, estimated limit of $3D \frac{S_2(r)}{r^2}$ as separation r goes to zero. Blue

diamond: $(\epsilon_Z)_{FD}$, FD method applied to the NF signal. Blue $*$: $(\epsilon_Z)_{Corr}$, correlation method applied to the NF signal. Blue solid line and diamonds: noise-corrected using structure functions. Magenta solid line and squares:

$3D \frac{S_2(r)}{r^2}$ from the W22 signal. Magenta circle: $(\epsilon_Z)_C$. Blue \bullet : $(\epsilon_Z)_{LS}$, large-scale method.

We have used four different methods in order to determine a correct value of $\overline{\epsilon_Z}$: finite differences, structure functions, correlation and large-scales. Good agreement between the values of $(\epsilon_Z)_{LS}$, $(\epsilon_Z)_C$, $(\epsilon_Z)_{Corr}$ and $(\epsilon_Z)_{SF}$ is obtained, the relative difference is of about 15%. That suggests that the methods permit a reliable estimate of the actual value of the mean scalar dissipation rate. A very last analysis of Figure 9 leads to the

conclusion that either $(\epsilon_Z)_C$ or $(\epsilon_Z)_{LS}$ are also well-approximated by the value of $\overline{\epsilon_Z}$ inferred from the NF signal, with a 1-pixel separation. This surprising conclusion was not obvious *a priori*, since the optimal separation chosen to infer small-scale characteristics strongly depends on flow Reynolds number, energy-injection mode, large-scale properties, etc.

CONCLUSIONS

Simultaneous PIV and acetone PLIF measurements have been performed in a Partially Stirred Reactor (PaSR), in which the fluid is injected via 12 jets situated in the upper and lower sides of the reactor. The experimental set-up is designed to reproduce, as best as possible, the central zone of a HCCI engine, in which different combustion models are to be, as final aim of this work, either tested, improved or developed.

The paper provides an experimental, global, characterisation of the PaSR, operating in a non-reactive regime. A global characterization of the flow signifies that different quantities are integrated in space/time over the whole of the images and at all points of the measurement zone. Global homogeneity and isotropy are roughly verified, though local inhomogeneity still persists. The Taylor microscale Reynolds number is relatively low ($R_\lambda \cong 80$) and the turbulence intensity is very high (up to 100%). Due to the small dimensions of the experimental set-up, the characteristic scales of the flow and mixing are very comparable with the injection scales (e.g. the diameters of the injection jets). This is obviously a consequence of the dependence on the initial conditions.

The main focus of this work was to provide an estimation, as exact as possible, of the mean dissipation rate of the passive scalar fluctuations, $\overline{\epsilon_Z}$. For that, difficulties are encountered because our measurements suffer of two pathologies. The first one is the noise (mainly induced by the camera) present at small scales, thus affecting the small-scale quantities such as $\overline{\epsilon_Z}$. The second one is the fact that the smallest measured scale (one pixel) is larger than the smallest scale of the flow (and of the mixing).

In order to noise decontaminate the images, different filters have been tested. We mainly discussed here the Wiener filter, applied to a cell defined by 2×2 pixels. Spectral analysis showed that the Wiener filtered signal (W22) is more adapted to correctly describe small scales, than the non-filtered signal (NF).

As a second step, and mainly because of the fact that the smallest scales are not measured, either the correlation method (based on the osculating parabola) or the finite difference method, are both applied to the NF signal. It is shown that these are not perfectly reliable.

More trust is conveyed to the value of $\overline{\epsilon_Z}$ obtained from the W22 signal and the structure functions method, when the separation r goes to zero. This last value is in good agreement (15 % difference) with $(\epsilon_Z)_{LS}$, obtained from the large-scales energy budget equation over the whole PaSR.

Note finally that our measurements do not provide any perfectly reliable value of $\overline{\epsilon_Z}$. However, the four different methods we have tested (each of them presenting some worth and shortcomings) lead to relatively close values of the mean dissipation rate.

As a further step, a similar treatment for any transport equation will allow various micro-mixing models (IEM, Curl, Curl modified, and more recent models) to be tested. A much later aim of this work is to test different micro-mixing models against measurements performed in a hot reacting configuration of the PaSR, better describing the HCCI engines. In this perspective, and mainly because of the very important dilatation at high temperatures and pressures, the experimental set-up will need to be redesigned. The measurement techniques would also need to be adapted to this much more complex situation.

Support of the French Minister of Research and Education (under grant ACI 'Jeunes Chercheurs' No 035181, 'Influence du micromélange pour les nouveaux systèmes de combustion') is gratefully acknowledged.

REFERENCES

- [1] Anselmet F, Djeridi H. and Fulachier L. (1994) Joint statistics of a passive scalar and its dissipation in turbulent flows, *Journal of Fluid Mechanics*, Vol. 280, pp. 173-197.
- [2] Birouk M., Sahr B. and Gokalp I. (2003) An attempt to realize experimental isotropic turbulence at low Reynolds numbers, *Flow Turbulence and Combustion*, Vol. 70, pp. 325-348.
- [3] Brunel M., Büleud O., Coëtmellec S., Lebrun D. and Özkul C. (2002) Optical limiting by digital restoration of defocused images, *Optics Communications*, Vol. 208, pp. 25-29.
- [4] Bryant R.A., Donbar J.M. and Driscoll J.F. (2000) Acetone laser induced fluorescence for low pressure/low temperature flow visualization, *Experiments in Fluids*, Vol. 28, pp. 471-476.
- [5] Christensen M., Johansson B., Amneus P. and Mauss F. (1998) Supercharged HCCI engines, *SAE Paper 980787*.
- [6] Comte-Bellot G. and Corrsin S. (1966) The use of a contraction to improve the isotropy of grid-generated turbulence, *Journal of Fluid Mechanics*, Vol. 25, pp. 657-682.
- [7] Correa S.M. (1993) Turbulence-chemistry interactions in the intermediate regime of premixed combustion, *Combustion and Flame*, Vol. 93, pp.41-60.
- [8] Danaila L., Zhou T., Anselmet F. and Antonia R.A. (2000) Calibration of a temperature dissipation probe in decaying grid turbulence, *Experiments in Fluids*, Vol. 28, pp. 45-50.
- [9] Elsner J.W., Domagala P. et Elsner W. (1993) Effect of spatial resolution of hot-wire anemometry on measurements of turbulence energy dissipation, *Meas. Sci. Technol.*, Vol. 4, pp. 517.
- [10] Hwang W. and Eaton J.K. (2003) Creating an homogeneous and isotropic turbulence without a mean flow, *Experiments in Fluids*, published online.
- [11] Lozano A., Yip B. and Hanson R.K. (1992) Acetone: a tracer for concentration measurements in gaseous flows by planar laser-induced fluorescence. *Experiments In Fluids*, Vol. 13, pp. 369-376.
- [12] Mydlarski L. and Warhaft Z. (1996) On the onset of high-Reynolds -number wind tunnel turbulence. *Journal of Fluid Mechanics*, Vol. 320, pp. 331-368.
- [13] Pao Y.H. (1965), Structure of turbulent velocity and scalar fields at large wave-numbers, *Physics of Fluids*, Vol. 8, pp. 1063.
- [14] Ren Z. and Pope S.B. (2004) An investigation of the performance of turbulent mixing models, *Combustion and Flame*, Vol. 136, pp. 208-216.
- [15] Van Cruyningen I, Lozano A. and Hanson R.K. (1990) Quantitative imaging of concentration by planar laser-induced fluorescence, *Experiments in Fluids*, Vol. 10, pp. 41-49.